Photometric and Spectroscopic Observations of GRB 190106A: Emission from Reverse and Forward Shocks with Late-time Energy Injection

Zi-Pei Zhu, Dong Xu, Johan P.U Fynbo, Shao-Yu Fu, Xing Liu, Shuai-Qing Jiang, Shuo Xiao, Wei Xie, Yuan-Chuan Zou, He Gao, et al.

The Astrophysical Journal, 948:30 (14pp), 2023 May 1 https://doi.org/10.3847/1538-4357/acbd96

Photometric and Spectroscopic Observations of GRB 190106A: Emission from Reverse and Forward Shocks with Late-time Energy Injection

Zi-Pei Zhu[1,2], Dong Xu[2], Johan P. U. Fynbo[3], Shao-Yu Fu[2,4], Jun-Bo Zhang[5], Xing Liu[2,6], Shuai-Qing Jiang[2,7], Shuo Xiao[8,9], Wei Xie[8], Yuan-Chuan Zou[1], He Gao[10], Dieter Hartmann[11], Antonio de Ugarte Postigo[12], David Alexander Kann[13], Massimo Della Valle[14,15,16], Pall Jakobsson[17], Tayyaba Zafar[18,19], Valerio D'Elia[20,21], Li-Ping Xin[2], Jian-Yan Wei[2,4], Xing Gao[22], Jin-Zhong Liu[2,22], Tian-Hua Lu[2,4], and Wei-Hua Lei[1]

[1] Department of Astronomy, School of Physics, Huazhong University of Science and Technology, Wuhan, 430074, People's Republic of China; leiwh@hust.edu.cn
[2] Key Laboratory of Space Astronomy and Technology, National Astronomical Observatories, Chinese Academy of Sciences, Beijing, 100101, People's Republic of China; dxu@nao.cas.cn
[3] The Cosmic Dawn Centre (DAWN), Niels Bohr Institute, University of Copenhagen, Lyngbyvej 2, DK-2100, Copenhagen, Denmark
[4] School of Astronomy and Space Science, University of Chinese Academy of Sciences, Chinese Academy of Sciences, Beijing 100049, People's Republic of China
[5] CAS Key Laboratory of Optical Astronomy, National Astronomical Observatories, Chinese Academy of Sciences, Beijing 100101, People's Republic of China
[6] Key Laboratory of Cosmic Rays, Ministry of Education, Tibet University, Lhasa, Tibet 850000, People's Republic of China
[7] University of Chinese Academy of Sciences, Chinese Academy of Sciences, Beijing 100049, People's Republic of China
[8] Guizhou Provincial Key Laboratory of Radio Astronomy and Data Processing, Guizhou Normal University, Guiyang, 550001, People's Republic of China
[9] School of Physics and Electronic Science, Guizhou Normal University, Guiyang, 550001, People's Republic Of China
[10] Department of Astronomy, Beijing Normal University, Beijing 100875, People's Republic of China
[11] Department of Physics and Astronomy, Clemson University, Clemson, SC29634, USA
[12] Université Côte d'Azur, Observatoire de la Côte d'Azur, Artemis, CNRS, F-06304 Nice, France
[13] Hessian Research Cluster ELEMENTS, Giersch Science Center, Max-von-Laue-Strasse 12, Goethe University Frankfurt, Campus Riedberg, D-60438 Frankfurt am Main, Germany
[14] Capodimonte Astronomical Observatory, INAF-Napoli, Salita Moiariello 16, Italy
[15] Department of Physics, Ariel University, Ariel, Israel
[16] Icranet, Piazza della Repubblica 10, I-65122 Pescara, Italy
[17] Centre for Astrophysics and Cosmology, Science Institute, University of Iceland, Dunhagi 5, 107, Reykjavik, Iceland
[18] Australian Astronomical Optics, Macquarie University, 105 Delhi Road, North Ryde, NSW 2113, Australia
[19] Macquarie University Research Centre for Astronomy, Astrophysics & Astrophotonics, Sydney, NSW 2109, Australia
[20] ASI-Space Science Data Centre, Via del Politecnico snc I-00133, Rome, Italy
[21] INAF Osservatorio Astronomico di Roma, Via di Frascati 33, I-00040, Monteporzio Catone, Rome, Italy
[22] Xinjiang Astronomical Observatory, Chinese Academy of Sciences, Urumqi, Xinjiang 830011, People's Republic of China
Received 2022 November 17; revised 2023 February 9; accepted 2023 February 14; published 2023 May 3

Abstract

Early optical observations of gamma-ray bursts can significantly contribute to the study of the central engine and physical processes therein. However, of the thousands observed so far, only a few have data at optical wavelengths in the first minutes after the onset of the prompt emission. Here we report on GRB 190106A, whose afterglow was observed in optical bands just 36 s after the Swift/BAT trigger, i.e., during the prompt emission phase. The early optical afterglow exhibits a bimodal structure followed by a normal decay, with a faster decay after $\sim T_0 + 1$ day. We present optical photometric and spectroscopic observations of GRB 190106A. We derive the redshift via metal absorption lines from Xinglong 2.16 m/BFOSC spectroscopic observations. From the BFOSC spectrum, we measure $z = 1.861 \pm 0.002$. The double-peak optical light curve is a significant feature predicted by the reverse-forward external-shock model. The shallow decay followed by a normal decay in both the X-ray and optical light curves is well explained with the standard forward-shock model with late-time energy injection. Therefore, GRB 190106A offers a case study for GRB emission from both reverse and forward shocks.

Unified Astronomy Thesaurus concepts: Gamma-ray bursts (629)

1. Introduction

Since their discovery in the 1960s, the understanding of gamma-ray bursts (GRBs) has been greatly advanced by various space satellites and ground-based telescopes (see Zhang 2018, for a review). Based on statistics of their prompt emission, GRBs are divided into two categories defined by their T_{90} duration and spectral hardness, i.e., short bursts with hard spectra (also called type I bursts) with $T_{90} < 2$ s and long bursts with soft spectra (also called type II bursts) with $T_{90} > 2$ s (Kouveliotou et al. 1993; Zhang et al. 2009). The association of the short GRB 170817A with the gravitational wave event GW170817 confirmed the longstanding prediction (Eichler et al. 1989) that neutron star mergers can indeed produce short bursts (Abbott et al. 2017a, 2017b; Zhang et al. 2018). Long GRBs are generally believed to originate from massive star collapse (Woosley & Bloom 2006). GRB 980425/SN 1998bw demonstrated that some stellar collapses produce long bursts and broad-lined Type Ic supernovae (SNe; Galama et al. 1999). The comparison between long-duration GRBs and broad-line supernova (SN) rates suggests the ratio GRBs/CC-SNe is approximately a few per thousand (Guetta & Della Valle 2007).

Recent observations suggest that collapsing stars can also produce GRBs that last shorter than 2 s (Ahumada et al. 2021;

Zhang et al. 2021; Rossi et al. 2022), compact star mergers seem to be also able to produce long GRBs (Rastinejad et al. 2022), indicating that classification of GRBs is more complex than the simple temporal division. Since its launch in 2004, the Neil Gehrels Swift Observatory (Swift hereafter) has detected more than 1700 GRBs with accurate positions, enabling easy follow-up observations with ground-based telescopes (Gehrels et al. 2004). The typical isotropic equivalent energy (since it is the energy equivalent to the one that the GRB should have if the emission were isotropic) of GRBs ranges between 10^{50} and 10^{54} erg within a few seconds to minutes (Atteia et al. 2017). The jet break predicted by the collimated jet model has been observed in some GRBs, leading to the estimates of the true energy being 2–3 orders of magnitude lower than the isotropic energy release (Frail et al. 2001).

Previous studies have shown that the X-ray light curves of GRB afterglows typically have several stages of power-law decay ($F \propto t^{-\alpha}$): a steep decay phase (typically $\alpha \sim 3$), a shallow decay phase also called a plateau (typically $\alpha \sim 0.5$), a normal decay phase (typically $\alpha \sim 1.2$), a post-jet-break phase (typically $\alpha \gtrsim 2$), with some bursts also accompanied by flares (Zhang et al. 2006). The typical optical light curve is an early rise followed by a normal decay, then sometimes followed by a rebrightening or a post-jet-break decay. Some long bursts, when at low enough redshift to allow a search, are found to be accompanied by an SN bump (Zeh et al. 2004; Li et al. 2012).

In the standard model of GRBs, the afterglow is believed to involve a relativistically expanding fireball. Considering a relativistic thin shell with energy $E_{\rm K}$, initial Lorentz factor Γ_0, opening angle $\theta_{\rm j}$, and a width in laboratory frame Δ_0 expanding into the interstellar medium (ISM) with density n, the interaction between the shell and ISM is described by two shocks: (1) a forward shock (FS) propagating into the ISM. The shell first undergoes a coasting phase, where it moves at a nearly constant speed $\Gamma(t) \simeq \Gamma_0$. It starts to decelerate and evolves into the second stage when the mass of the ISM swept by the FS is about $1/\Gamma_0$ of the rest mass of the shell. The third phase is the post-jet-break phase when the $1/\Gamma$ cone becomes larger than the geometric cone defined by $\theta_{\rm j}$. Finally, the blast wave enters the Newtonian phase (its velocity is much smaller than the speed of light) when it has swept up the ISM with the total rest mass energy comparable to the energy of the shell. During all these three phases, electrons are believed to be accelerated at the FS front to a power-law distribution $N(\gamma_{\rm e}) \propto \gamma_{\rm e}^{-p_{\rm f}}$. A fraction $\epsilon_{\rm e,f}$ of the shock energy is distributed into electrons, and a fraction $\epsilon_{\rm B,f}$ is in the magnetic field generated behind the shock. Accounting for the radiative cooling and the continuous injection of new accelerated electrons at the shock front, one expects a broken power-law energy spectrum of them, which leads to a multi-segment broken power-law radiation spectrum at any epoch (see Gao et al. 2013, for a review). The typical afterglow observations are successfully described by the synchrotron emission of electrons from the FSs. However, the information on the properties of the fireball is lost in the FS, especially when it has been decelerated by the ISM; (2) a reverse shock (RS) propagating into the shell, which occurs in the very early afterglow epoch. In the thin shell case, the RS is too weak to decelerate the shell effectively. The Lorentz factor of the emission phase, showing a double-peak shocked shell material is almost constant while the shock propagates in the shell. The RS crosses the shell at the fireball deceleration time. At this time, the reverse-shocked and forward-shocked regions have the same Lorentz factor and internal energy density. However, the typical temperature of RS is lower since the mass density of the shell is higher. Consequently, the typical frequency of RS is lower, and RS may play a noticeable role in the low-frequency bands, e.g., optical or radio (Mészáros & Rees 1997). After the RS crosses the shell, the Lorentz factor of the shocked shell may be assumed to have a general power-law decay behavior $\gamma_3 \propto r^{-g}$. The shell expands adiabatically in the shell's comoving frame. The emission from the RS is sensitive to the properties of the fireball. Observations of RS can thus provide important clues on the nature of the GRB source.

Catching very early (a few minutes after the trigger) optical emission from GRBs is not an easy task. There are only a few GRBs with optical observations during the prompt phase (Gao & Mészáros 2015, for a review). Oganesyan et al. (2019) provided a sample of 21 GRBs with at least one observation during the prompt emission phase, and several GRBs in the sample are well observed (e.g., GRB 070616, GRB 081008, and GRB 121217A). Recently, Oganesyan et al. (2021) reported that they began to observe GRB 210619B ~ 28 s after the Swift trigger with a D50 clear band during the prompt emission phase. However, our understanding of the earlier phases of GRBs continues to be quite incomplete compared to the later afterglow phases (occurring tens of minutes after the trigger).

In this paper, we report a special burst, GRB 190106A, for which optical observations began during the prompt emission phase, showing a double-peaked early optical light curve. We present optical photometric and spectroscopic observations of GRB 190106A with the NEXT (Ningbo Bureau of Education and Xinjiang Observatory Telescope) and the Xinglong 2.16 m telescopes. With the Xinglong 2.16 m/BFOSC spectroscopic observation, we present the redshift and calculate the equivalent widths (EWs) of absorption lines in the afterglow spectrum. Combining our data with the Swift/XRT data and other observations from GRB Coordinates Network (GCN) reports, we constrain the parameters in an external-shock model of the afterglow.

Our observations and data reduction are described in Section 2. The spectroscopic data analysis and redshift measurements are presented in Section 3. The optical and X-ray afterglow data analysis and the modeling of the afterglow light curve are reported in Section 4. We discuss possible models and present our conclusions in Section 5 and Section 6, respectively. A standard cosmology model is adopted with $H_0 = 67.3\,{\rm km\cdot s^{-1}\,Mpc^{-1}}$ and $\Omega_M = 0.315$, $\Omega_\Lambda = 0.685$ (Planck Collaboration et al. 2014).

2. Observations

GRB 190106A triggered Neil Gehrels Swift Observatory (Swift) Burst Alert Telescope (BAT; Barthelmy et al. 2005) at 13:34:44 UT on 2019 January 6 (Sonbas et al. 2019). It is a long-duration burst with $T_{90} = 76.8 \pm 2.4$ s. Konus-Wind also detected the burst with $T_{90} = 77.1^{+1.3}_{-4.2}$ s (Tsvetkova et al. 2019). The MASTER-Amur robotic telescope quickly slewed to the burst position, starting observations 36 s after the BAT trigger. An optical transient (with a magnitude of 15.23 in the P band) was discovered within the Swift/BAT error circle in the second 10 s exposure image (Lipunov et al. 2019; Yurkov et al. 2019) located

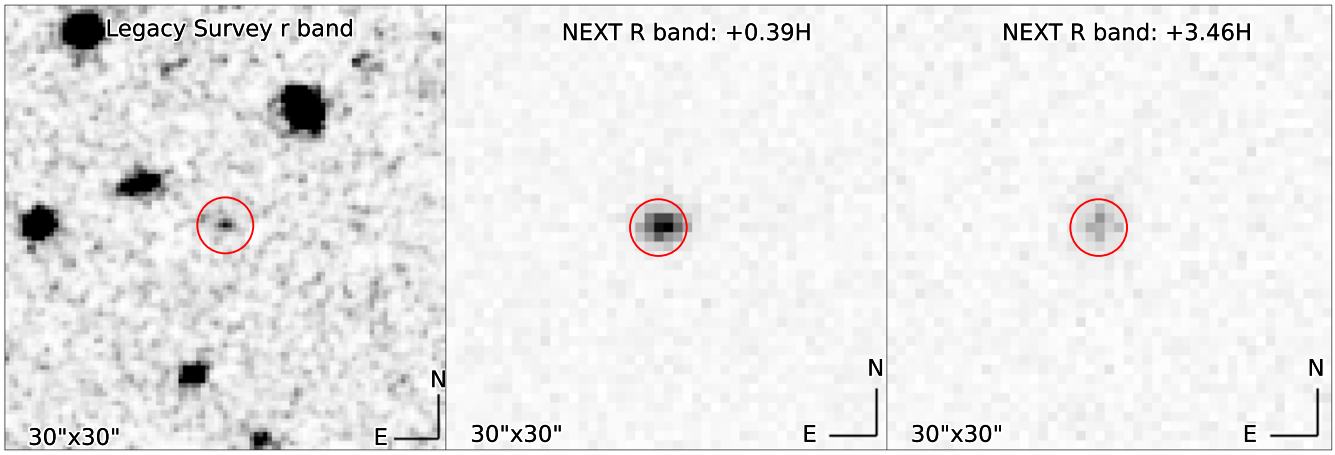

Figure 1. The *R*-band position of GRB 190106A within the the FOV 30″ × 30″. The location of the burst is circled in red. North is up and east is left. Left panel: the DESI Legacy Imaging Surveys *r*-band image (Dey et al. 2019). A weak but obvious source with $r \sim 24.0$ mag is located at the GRB position, which could be the host galaxy of the burst. Middle panel: the first NEXT image, obtained 0.39 hr after the BAT trigger, shows a bright source consistent with the UVOT coordinates with $R = 16.9$ mag. Right panel: the NEXT image obtained at 3.46 hr after the burst. The source in the image center is obviously fainter than the one in the middle panel, with a brightness of $R = 18.4$ mag.

at equatorial coordinates (J2000.0): R. A. $= 1^{h}59^{m}31\overset{s}{.}19$, decl. $= +23°50'44\overset{''}{.}79$, consistent with the Swift/UVOT position R. A. $= 01^{h}59^{m}31\overset{s}{.}18$, decl.$= +23°50'44\overset{''}{.}0$ (Kuin & Sonbas 2019). XRT and UVOT started observations at 81.8 and 90 s after the BAT trigger, respectively. The BAT data files were downloaded from the Swift data archive.[23] We extracted the BAT light curve and spectrum by the *HEASoft* software package (v6.27.2). The 15–150 keV spectra are analyzed in *XSPEC* (version 12.12) with power-law approximation over the time interval from 71–81 s after the BAT trigger. We adopted the analysis results of the XRT repository products (Evans et al. 2007, 2009) and downloaded the 0.3–10 keV unabsorbed light curve from the UK Swift Science Data Center.[24]

In our subsequent ground-based optical follow-up observations, the Xinglong 2.16 m obtained spectroscopic observations from which the redshift was determined (Xu et al. 2019), also confirmed by GMG (Mao et al. 2019) and X-shooter (Schady et al. 2019). We also collected observations from the GCNs reported by MASTER (Lipunov et al. 2019) and Sayan Observatory, Mondy (Belkin et al. 2019a, 2019b). The MASTER data are converted to the *R* band by adding $\Delta R = 0.51$ mag following Xin et al. (2018). The corrected MASTER magnitude and Mondy optical observations are shown in Figure 2 in gray.

2.1. NEXT Optical Observations

NEXT is a fully automated telescope with a diameter of 60 cm, located at Nanshan, Xingming Observatory. NEXT is equipped with an E2V 230–42 back-illuminated CCD, and the CCD controller was made by the Finger Lakes Instrumentation (FLI). The size of the CCD is 2048 × 2048 pixels, with a pixel size of 15 μm. The pixel scale is $0\overset{''}{.}64$ pixel^{-1}, and the field of view (FOV) is $22' \times 22'$ according to the size of the CCD. The typical gain is $1.85e^{-}$/ADU, and typical readout noise is $13e^{-}$ with a 500 kHz readout speed. The equipped filters were in the standard Johnson–Cousins system.

NEXT is connected to the GCN/TAN alert system, but did not observe GRB 190106A immediately as the dome was still closed at the very beginning of the event. NEXT began to obtain the first image at 13:57:21 UT, 22.6 minutes after the BAT trigger, and the final one ended at 20:09:26 UT when the airmass was ∼9. The NEXT image of the burst location is also shown in Figure 1. We obtained 88 images, all in the R_C filter. Five of them were discarded for poor quality. The observing center time and exposure time of each image used are presented in Table 1.

The data reduction was carried out by standard processes in the IRAF packages (Tody 1986), including bias, flat, and dark current corrections. The cosmic rays were also removed by the filtering described in van Dokkum (2001). The final five useful images were combined using the *imcombine* task in IRAF. The astrometry was calibrated using Astrometry.net (Lang et al. 2010). The magnitudes were measured using SourceExtractor (Bertin & Arnouts 1996) using a circular aperture with a nine-pixel diameter. The photometric calibration was derived using the Sloan Digital Sky Survey (SDSS) 14th data release (Abolfathi et al. 2018), with flux/mag conversion of the SDSS system into the Johnson–Cousins system.[25] The light curve is shown in Figure 2 and the photometric results are presented in Table 1.

2.2. Xinglong 2.16 m Observations

The spectroscopic observations were carried out with the National Astronomical Observatories, Chinese Academy of Sciences (NAOC) 2.16 m telescope (Fan et al. 2016) in Xinglong Observatory on 2019 January 6 at 14:02:39, 27.9 minutes after the BAT trigger. The optical spectrum was obtained with the Beijing Faint Object Spectrograph and Camera (BFOSC) equipped with a back-illuminated E2V55-30 AIMO CCD. The optical afterglow magnitude was ∼16 mag in the *R* band and the airmass was approximately 1.3 at the beginning of the spectroscopic observations. Due to a seeing of about 2″ a slit-width of $1\overset{''}{.}8$ was used. The slit was oriented in the south–north direction. The grating used was G4 and the order-sorter filter 385LP was also used, leading to a spectral coverage of 3800–9000 Å at a resolution of about 10 Å. A total

[23] https://www.swift.ac.uk/swift_portal/
[24] https://www.swift.ac.uk/xrt_curves/
[25] https://www.sdss.org/dr12/algorithms/sdssUBVRITransform/#Lupton

Table 1
Photometric Results of NEXT and Xinglong 2.16 m

$T_{\rm mid}$ (s)	Exp (s)	Filter	Mag (Vega)	Telescope	$T_{\rm mid}$ (s)	Exp (s)	Filter	Mag (Vega)	Telescope
1387	60	*R*	16.92 ± 0.02	NEXT	10661	200	*R*	18.27 ± 0.04	NEXT
1482	60	*R*	16.98 ± 0.02	NEXT	11109	200	*R*	18.39 ± 0.05	NEXT
1569	60	*R*	17.01 ± 0.02	NEXT	11337	200	*R*	18.41 ± 0.05	NEXT
1673	90	*R*	17.05 ± 0.02	NEXT	11564	200	*R*	18.36 ± 0.05	NEXT
1786	90	*R*	17.10 ± 0.02	NEXT	11791	200	*R*	18.40 ± 0.05	NEXT
1898	90	*R*	17.11 ± 0.02	NEXT	12017	200	*R*	18.39 ± 0.05	NEXT
2068	200	*R*	17.24 ± 0.01	NEXT	12239	200	*R*	18.42 ± 0.05	NEXT
2291	200	*R*	17.30 ± 0.02	NEXT	12462	200	*R*	18.42 ± 0.05	NEXT
2513	200	*R*	17.42 ± 0.02	NEXT	12733	300	*R*	18.47 ± 0.04	NEXT
2786	300	*R*	17.45 ± 0.02	NEXT	13052	300	*R*	18.45 ± 0.04	NEXT
3105	300	*R*	17.53 ± 0.02	NEXT	13370	300	*R*	18.41 ± 0.05	NEXT
3425	300	*R*	17.64 ± 0.02	NEXT	13688	300	*R*	18.43 ± 0.05	NEXT
4063	300	*R*	17.76 ± 0.02	NEXT	14005	300	*R*	18.50 ± 0.05	NEXT
4388	300	*R*	17.80 ± 0.02	NEXT	14321	300	*R*	18.52 ± 0.05	NEXT
4654	120	*R*	17.77 ± 0.03	NEXT	14637	300	*R*	18.47 ± 0.04	NEXT
4799	120	*R*	17.84 ± 0.03	NEXT	14955	300	*R*	18.55 ± 0.05	NEXT
4945	120	*R*	17.86 ± 0.03	NEXT	15272	300	*R*	18.62 ± 0.05	NEXT
5089	120	*R*	17.90 ± 0.03	NEXT	15589	300	*R*	18.61 ± 0.06	NEXT
5236	120	*R*	17.94 ± 0.04	NEXT	15905	300	*R*	18.69 ± 0.06	NEXT
5381	120	*R*	17.90 ± 0.03	NEXT	16222	300	*R*	18.63 ± 0.05	NEXT
5529	120	*R*	17.92 ± 0.03	NEXT	16539	300	*R*	18.54 ± 0.05	NEXT
5675	120	*R*	17.98 ± 0.04	NEXT	16855	300	*R*	18.48 ± 0.05	NEXT
5912	200	*R*	18.00 ± 0.03	NEXT	17172	300	*R*	18.62 ± 0.06	NEXT
6138	200	*R*	17.97 ± 0.03	NEXT	17489	300	*R*	18.52 ± 0.05	NEXT
6363	200	*R*	18.04 ± 0.03	NEXT	17806	300	*R*	18.59 ± 0.06	NEXT
6589	200	*R*	18.01 ± 0.03	NEXT	18123	300	*R*	18.61 ± 0.07	NEXT
6813	200	*R*	18.09 ± 0.03	NEXT	18440	300	*R*	18.41 ± 0.06	NEXT
7042	200	*R*	18.05 ± 0.03	NEXT	18756	300	*R*	18.68 ± 0.07	NEXT
7267	200	*R*	18.10 ± 0.03	NEXT	19074	300	*R*	18.64 ± 0.07	NEXT
7491	200	*R*	18.14 ± 0.03	NEXT	19391	300	*R*	18.63 ± 0.07	NEXT
7717	200	*R*	18.12 ± 0.03	NEXT	19709	300	*R*	18.84 ± 0.09	NEXT
7946	200	*R*	18.16 ± 0.03	NEXT	20025	300	*R*	18.83 ± 0.10	NEXT
8172	200	*R*	18.12 ± 0.03	NEXT	20342	300	*R*	18.85 ± 0.10	NEXT
8397	200	*R*	18.12 ± 0.03	NEXT	20658	300	*R*	18.75 ± 0.10	NEXT
8624	200	*R*	18.23 ± 0.04	NEXT	20975	300	*R*	18.72 ± 0.10	NEXT
8852	200	*R*	18.28 ± 0.04	NEXT	21292	300	*R*	18.96 ± 0.13	NEXT
9078	200	*R*	18.30 ± 0.04	NEXT	21609	300	*R*	18.84 ± 0.12	NEXT
9302	200	*R*	18.28 ± 0.04	NEXT	21925	5 × 300	*R*	19.12 ± 0.12	NEXT
9529	200	*R*	18.32 ± 0.04	NEXT	84911	5 × 360	*R*	19.77 ± 0.06	Xinglong 2.16 m
9756	200	*R*	18.30 ± 0.04	NEXT	165878	7 × 360	*R*	20.70 ± 0.05	Xinglong 2.16 m
9980	200	*R*	18.31 ± 0.04	NEXT	345290	10 × 360	*R*	21.73 ± 0.06	Xinglong 2.16 m

Note. $T_{\rm mid}$ is the middle time of the exposure after the BAT Trigger. Exp is the exposure time. All data are calibrated using nearby SDSS reference stars and not corrected for Galactic extinction, which is $E(B-V)=0.08$ mag (Schlafly & Finkbeiner 2011).

of two spectra were obtained with exposure times of 3600 and 2400 s, respectively.

The BFOSC spectroscopic data were reduced by the IRAF standard processes to obtain clean images, including bias subtraction, flat-field correction, and cosmic-ray removal. With the use of the "NOAO" package provided in IRAF, we extracted the one-dimensional spectrum of the burst, and calibrated the wavelength with arc spectra from an iron-argon lamp. The flux calibration was performed by the standard star HD+19445 (Oke & Gunn 1983) obtained with the same instrumental setup on the same night. The extracted spectrum after the processing above is shown in Figure 3.

The photometric observations were carried out on January 7, 8, and 10 in the *R* filter again using the BFOSC (Fan et al. 2016). The exposure times were 5×360, 7×360, and 10×360 s, respectively. The data reduction and processing were the same as that used for NEXT, except for dark current, which was negligible. The subsequent magnitude measurements were also performed as described above. The photometric data are presented in Table 1 and shown in Figure 2. A comparison with a sample of historical GRB optical light curves is shown in Figure 4.

3. Spectroscopic Analysis

As the blue end of the BFOSC spectrum has a poor signal-to-noise ratio (S/N), our spectral analysis starts at 4300 Å. After excluding the *A*- and *B*-band absorption and sky emission lines, we identified the metal absorption lines detected at more than 3σ significance. We detected lines from C IV, Al II, Al III, Fe II, and Mg II. Line centroids were determined by fitting a Gaussian function to the line profiles. We obtain a redshift of $z=1.861\pm0.002$. The identified lines with the equivalent widths ($\rm EW_{obs}$) are listed in Table 2 and also shown in Figure 3.

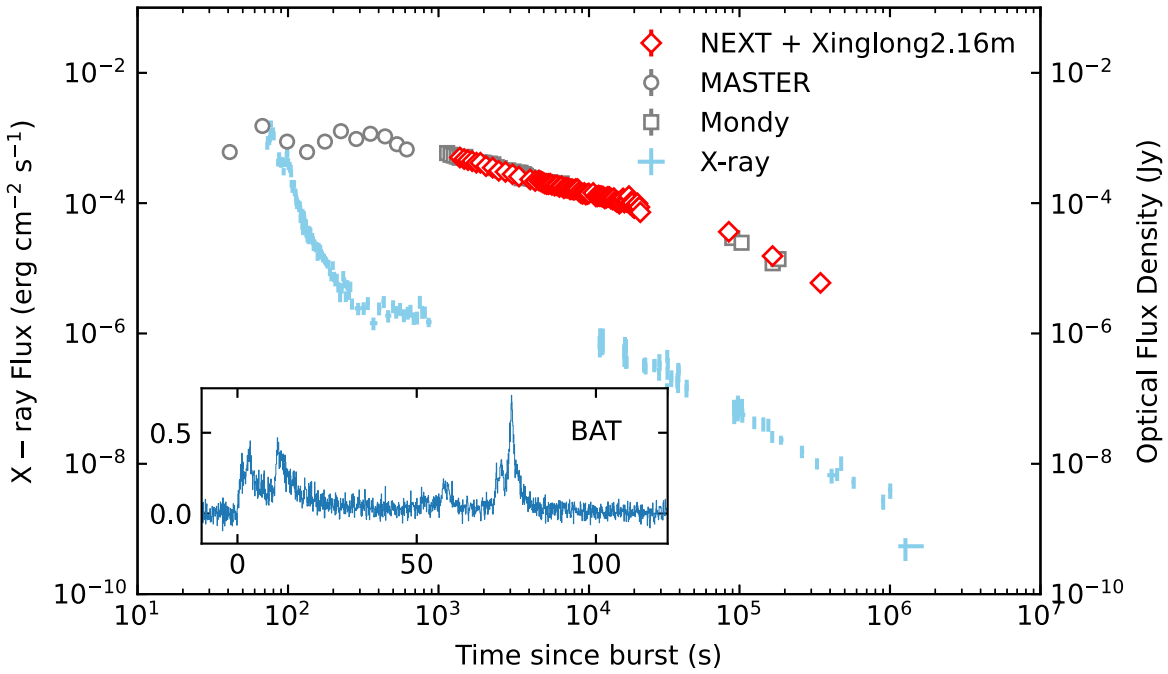

Figure 2. The light curves of GRB 190106A in γ-ray, X-ray, and optical *R* band. The X-ray light curve colored in cyan is 0.3–10 keV unabsorbed flux, obtained from UK Swift Science Data Center (Evans et al. 2009). The gray circles and gray squares are modified MASTER and Mondy photometric results, respectively. The red diamond points out our observations obtained by NEXT and Xinglong 2.16 m. Most of the error bars are smaller than the marker, and our photometric data are listed in Table 1.

3.1. Line Strength Analysis

We analyzed the strong features of the GRB host galaxy interstellar medium detected by BFOSC, following de Ugarte Postigo et al. (2012). The line strength parameter (LSP) of the spectrum is $\mathrm{LSP} = 0.15 \pm 0.18$, which is very similar to the average value of the sample presented in the paper above. The line strength of the burst compared with the sample is shown in Figure 5.

4. Optical and X-Ray Analysis and External-shock Modeling

4.1. Temporal Analysis

The *R* band, γ-ray, and X-ray at 10 keV light curves are shown in Figure 2. The optical light curve started at $T0 + 36$ s and ended at $T0 + 4.02$ days after the burst. According to the decay of the light curve, the optical and X-ray light curves can be divided into five and four stages, respectively. We fit the temporal indices α of the light curves in Figure 2 using $F \propto t^{-\alpha}$.

The optical afterglow of the *R*-band light curve can be divided into five stages with different decay indices, which are listed in Table 3, where the start and end times of different stages are also listed. The first stage is called fast rising, from the beginning of observation to ∼67 s after the burst. This is followed by a fast decay until $\sim 1.3 \times 10^2$ s. In the third stage (slow rising) it is still rising, and the index has decreased by about 1 compared with the first stage. The fourth stage, normal decay, starts at $\sim 2.8 \times 10^2$ s and continues to $\sim 7.7 \times 10^4$ s with a decay index of 0.63. In the final stage, late decay, the decay index increases to 1.29.

The light curve in X-rays seems simpler than in the optical, and can be divided into the stages directly. The first stage is the tail of the prompt emission (steep decay) with a decay index of ∼4.2, observations started at $T0 + 72.8$ s. This is followed by a shallow decay from $\sim 2.6 \times 10^1$ to $\sim 1.6 \times 10^4$ s, with an index of 0.36. This stage can also be called a plateau phase, resulting from the small index. In the final stage, which is called late decay, the decay index increased to ∼1.3.

The BAT (15–350 keV) count rates are also shown in Figure 2. The light curve can be simply divided into six episodes. The start, end, and peak times of each episode are shown in Table 4. We note that between ∼71 and ∼81 s of the prompt emission, the optical light curves have a similar evolutionary behavior: they all peak around 70 s and then fade. However, the peak time is slightly different, i.e., ∼76 s for γ-ray, ∼76 s for X-ray, and ∼68 s for optical. The two high energy bands are almost simultaneous, but the optics peak about 8 s earlier. In addition, the BAT and XRT spectrum of this period can be described using a single power law $F_\nu \propto \nu^{-\beta}$, and $\beta_{\mathrm{BAT}} = 0.77 \pm 0.04$, $\beta_{\mathrm{XRT}} = 0.72 \pm 0.10$, which is shown in Figure 6. Although the UVOT optical data are not included in the spectral fitting, they are shown in the best-fit spectra in Figure 6. As we can see, the optical data are much lower than the extrapolation of the best spectral fits for high energies. The spectral energy distribution (SED) containing optical and high energy (X-ray, γ-ray) cannot be fitted by a single power law.

4.2. Afterglow SED Analysis

To study the spectral energy properties of the afterglow, we select two epochs to construct its SED with the best multiband data: 28.8 ks (epoch 1) and 147.6 ks (epoch 2). The X-ray time sliced spectrum is obtained from the online repository,[26] and

[26] https://www.swift.ac.uk/xrt_spectra/

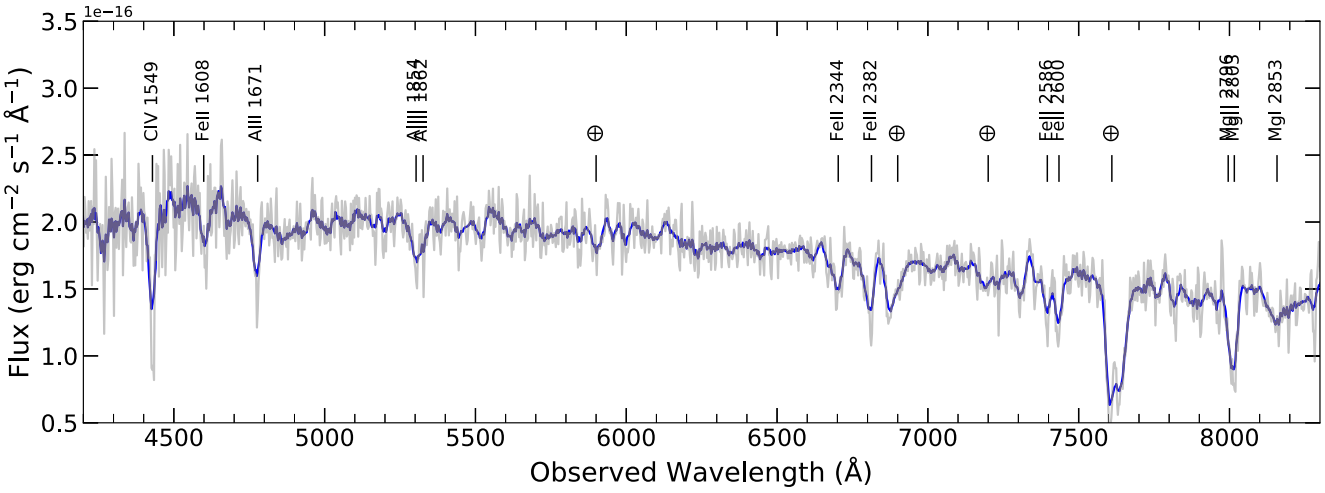

Figure 3. The spectrum obtained with the Xinglong 2.16 m/BFOSC. Gray denotes the original spectrum and the blue spectrum was smoothed for display purposes. The identified metal absorption lines are indicated with vertical lines in the figure. Telluric features are marked with the telluric symbol.

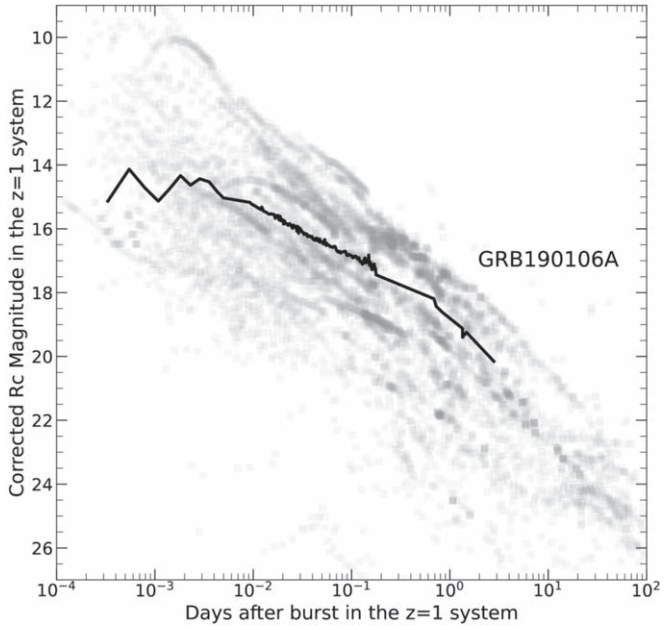

Figure 4. Comparison of a large sample of GRB optical afterglow light curves shifted in time and flux to a common redshift of $z = 1$ following Kann et al. (2010). The gray background represents historical data of other GRB light curves. GRB 190106A is shown as a black solid line, which lies in the middle of the distribution in terms of luminosity.

Table 2
Features in the Spectra and Their Observatory Frame EWs

λ_{obs}(Å)	Feature(Å)	z	EW$_{obs}$(Å)
4428.26	C IV/ C IV $\lambda\lambda$1549	1.859	8.68 ± 1.04
4604.72	Fe II $\lambda\lambda$1608	1.864	2.11 ± 0.63
4776.51	Al II $\lambda\lambda$1670	1.860	4.84 ± 0.55
5304.92	Al III $\lambda\lambda$1854	1.861	3.30 ± 0.49
5329.60	Al III $\lambda\lambda$1862	1.862	1.44 ± 0.35
6704.71	Fe II $\lambda\lambda$2344	1.860	4.25 ± 0.41
6789.60	Fe II $\lambda\lambda$2374	1.860	3.01 ± 0.45
6811.21	Fe II $\lambda\lambda$2382	1.859	7.52 ± 0.45
7397.92	Fe II $\lambda\lambda$2586	1.861	3.59 ± 0.55
7435.47	Fe II $\lambda\lambda$2600	1.860	5.45 ± 0.64
8011.58	Mg II/Mg II $\lambda\lambda$ 2800	1.861	14.14 ± 1.01
8158.45	Mg I $\lambda\lambda$ 2852	1.861	2.23 ± 0.44

the optical data are from Izzo et al. (2019) and Dichiara et al. (2019). We utilized the "grpph" tool of the Xspec package to rebin the X-ray data to guarantee that each bin contains at least 20 counts to improve the S/N. We fit the spectrum by the power-law function from "zdust*zphabs*phabs*powerlaw" model in the Xspec package, where "zdust" represents extinction by dust grains from the host galaxy of the burst, "zphabs" and "phabs" are neutral hydrogen photoelectric absorption of the host galaxy and Galaxy, respectively. The redshift and the Galactic hydrogen column is fixed to 1.86 and 7.1×10^{20} cm^{-2} (HI4PI Collaboration et al. 2016), respectively. Small Magellanic Cloud extinction law is used as the host galaxy extinction model. The best-fitted extinction $E(B-V)$ of the host galaxy is 0.1 for epoch 1, which is also fixed in the fit of epoch 2. The best-fitting result gives the photon index $\Gamma = -1.78 \pm 0.03$ and $\Gamma = -1.79 \pm 0.01$ for epochs 1 and 2, respectively. The results of these two epochs are shown in Figure 7.

4.3. Theoretical Interpretation

The afterglow light curve of GRB 190106A is unusual. There is an optical flash followed by a second bump in the early optical light curve, and then a shallow decay followed by a normal decay. The X-ray light curve shows a steeper decay at the end of the prompt emission, followed by a shallow decay, and finally a normal decay.

To understand the multiband observational data of GRB 190106A, we consider a relativistic thin shell with energy $E_{K,iso}$, initial Lorentz factor Γ_0, opening angle θ_j, and an initial width in laboratory frame Δ_0 expanding into the ISM with density n. The interaction between the shell and ISM is described by two shocks: an RS propagating into the shell and an FS propagating into the ISM (Rees & Meszaros 1992; Mészáros & Rees 1997; Sari et al. 1998; Sari & Piran 1999; Zou et al. 2005). There are four regions separated by the two shocks: Region 1, the ISM with density n_1; Region 2, the shocked ISM; Region 3, the shocked shell material; and Region 4, the unshocked shell material with density n_4. First, the pair of shocks (FS and RS) propagate into the ISM and the shell, respectively. After the RS crosses the shell, the blast wave enters the deceleration phase. We now briefly describe these shocks separately.

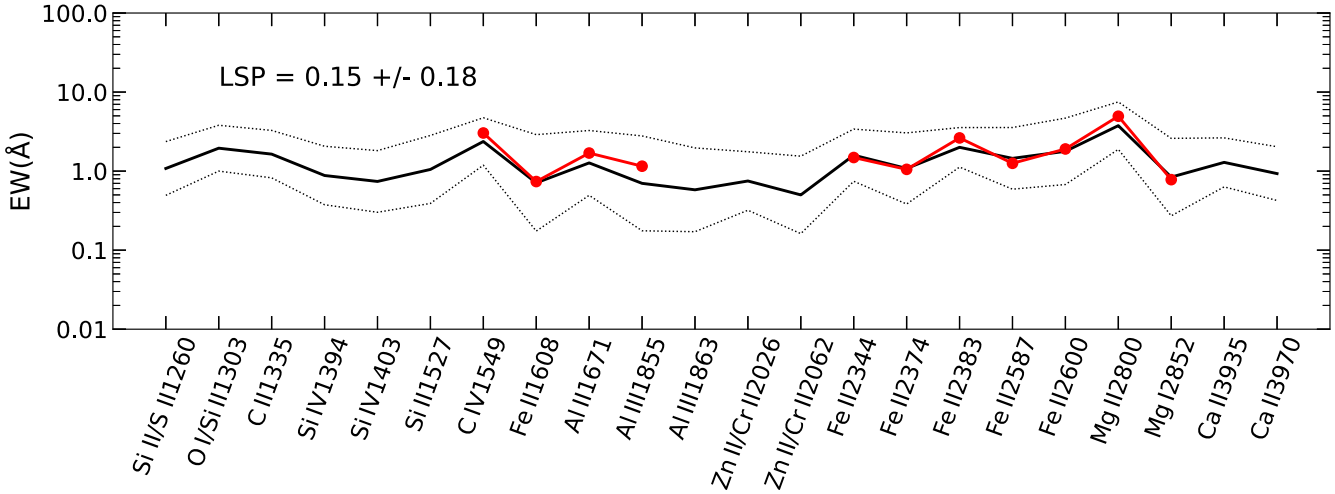

Figure 5. The EWs of GRB 190106A obtained from BFOSC are colored in red. These can be compared to the average and standard deviation of strengths of a sample of GRB afterglows in black, as described by de Ugarte Postigo et al. (2012).

Table 3
X-Ray and Optical Light-curve Decay Indices

Band	Segment	Start (s)	End (s)	α
X-ray	Steep decay	⋯	2.6×10^2	3.91 ± 0.25
	Shallow decay	2.6×10^2	1.6×10^4	0.36 ± 0.03
	Late decay	1.6×10^4	⋯	1.31 ± 0.03
Optical	Fast rising	⋯	6.7×10^1	-1.88 ± 0.57
	Fast decay	6.7×10^1	1.3×10^2	1.35 ± 0.32
	Slow rising	1.3×10^2	2.8×10^2	-0.58 ± 0.17
	Shallow decay	2.8×10^2	7.7×10^4	0.63 ± 0.01
	Late decay	7.7×10^4	⋯	1.29 ± 0.06

Table 4
Start, End, and Peak Times of Each Episode

Episode	Start (s)	End (s)	Peak (s)	Duration (s)
Episode 1	0.2	9.2	2.8	9.0
Episode 2	9.2	23.5	11.0	14.3
Episode 3	50.6	57.1	52.1	6.5
Episode 4	57.1	61.1	57.3	4.0
Episode 5	71.0	75.2	73.3	4.2
Episode 6	75.2	80.9	76.4	5.7

The FS model we adopt was described in Lei et al. (2016). The dynamical evolution of the shell is calculated numerically using a set of hydrodynamical equations (Huang et al. 2000)

$$\frac{dR}{dt} = \beta c\Gamma(\Gamma + \sqrt{\Gamma^2 - 1}), \tag{1}$$

$$\frac{dm}{dR} = 2\pi R^2(1 - \cos\theta_j)n_1 m_p, \tag{2}$$

$$\frac{d\Gamma}{dm} = -\frac{\Gamma^2 - 1}{M_{ej} + 2\Gamma m}, \tag{3}$$

where R and t are the radius and time of the event in the burster frame, m is the swept-up mass, $M_{ej} = E_{K,iso}(1 - \cos\theta_j)/2(\Gamma_0 - 1)c^2$ is the ejecta mass, m_p is the proton mass, and $\beta = \sqrt{\Gamma^2 - 1}/\Gamma$. The last equation could be replaced with (Geng et al. 2013)

$$\frac{d\Gamma}{dm} = -\frac{\Gamma^2 - 1 - \frac{1-\beta}{\beta c^3}L_{inj}dR/dm}{M_{ej} + 2\Gamma m}, \tag{4}$$

when there is energy injection from GRB central engine. For $t_{start} < t < t_{end}$, the injected power is $L_{inj} = L^0_{inj}(t/t_{start})^{-q}$, where L^0_{inj} is the initial injection power, q is the decay power-law index, and t_{start} and t_{end} are the start and end time for energy injection. By solving these equations with the initial conditions, one can find the evolution of $\Gamma(t)$ and $R(t)$.

During the dynamical evolution of FS, electrons are believed to be accelerated at the shock front to a power-law distribution of $N(\gamma_e) \propto \gamma_e^{-p_f}$. Assuming a fraction $\epsilon_{e,f}$ of the shock energy $e_2 = 4\Gamma^2 n_1 m_p c^2$ is distributed into electrons, this defines the minimum injected electron Lorentz factor,

$$\gamma_m = \frac{p - 2}{p - 1}\epsilon_{e,f}(\Gamma - 1)\frac{m_p}{m_e}, \tag{5}$$

where m_e is the electron mass. We also assume that a fraction $\epsilon_{B,f}$ of the shock energy is in the magnetic field generated behind the shock. This gives the comoving magnetic field

$$B = (32\pi m_p \epsilon_{B,f} n_1)^{1/2} c. \tag{6}$$

The synchrotron power and characteristic frequency from electron with Lorentz factor γ_e are

$$P(\gamma_e) \simeq \frac{4}{3}\sigma_T c\Gamma^2\gamma_e^2\frac{B^2}{8\pi}, \tag{7}$$

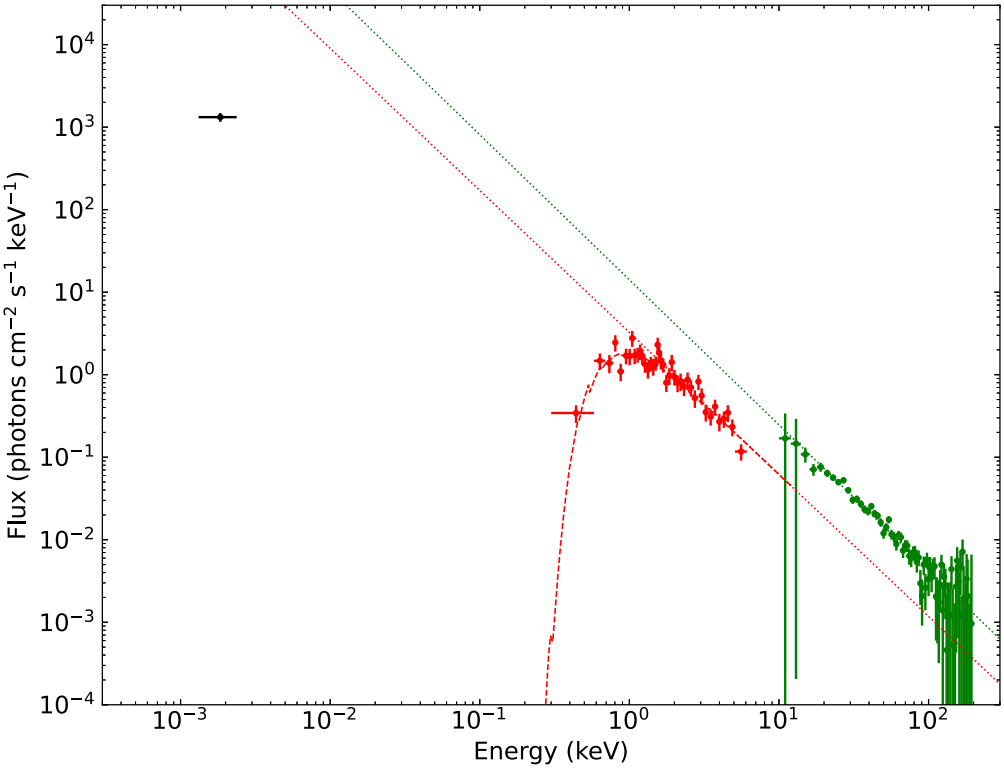

Figure 6. The prompt phase SED combined with optical (black), XRT (red), and BAT (green). The BAT time interval ranges from 71–81 s, while the XRT ranges from 85–95 s. The satellite was still slewing before 85 s, so the XRT data before 85 s are ignored. The optical point is converted from the MASTER observation and not included in the fitting. The data points of BAT and XRT were fitted with a single power-law function, and the spectral indices are 0.77 ± 0.04 and 0.72 ± 0.10, respectively.

$$\nu(\gamma_{\rm e}) \simeq \Gamma\gamma_{\rm e}^2 \frac{q_{\rm e}B}{2\pi m_{\rm e}c}, \tag{8}$$

where $\sigma_{\rm T}$ is the Thomson cross section, and $q_{\rm e}$ is the electron charge. The peak spectra power occurs at $\nu(\gamma_{\rm e})$

$$P_{\nu,\max} \simeq \frac{P(\gamma_{\rm e})}{\nu(\gamma_{\rm e})} = \frac{m_{\rm e}c^2\sigma_{\rm T}}{3q_{\rm e}}\Gamma B. \tag{9}$$

By equating the lifetime of the electron to the time t, one can define a critical electron Lorentz factor $\gamma_{\rm c}$

$$\gamma_{\rm c} = \frac{6\pi m_{\rm e}c}{\Gamma\sigma_{\rm T}B^2 t}, \tag{10}$$

and the electron distribution shape should be modified for $\gamma_{\rm e} > \gamma_{\rm c}$ when cooling due to synchrotron radiation becomes significant. Accounting for the radiative cooling and the continuous injection of new accelerated electrons at the shock front, one expects a broken power-law energy spectrum of them, which leads to a multi-segment broken power-law radiation spectrum separated by three characteristic frequencies at any epoch (Gao et al. 2013, see Equations (15)–(17) therein). The first two characteristic frequencies $\nu_{\rm e}$ and $\nu_{\rm c}$ in the synchrotron spectrum are defined by the two electron Lorentz factors $\gamma_{\rm e}$ and $\gamma_{\rm c}$. The third characteristic frequency is the self-absorption frequency $\nu_{\rm a}$, below which the synchrotron photons are self-absorbed (self-absorption optical depth larger than unity). The maximum flux density is $F_{\nu,\max,{\rm f}} = N_{\rm e,2}P_{\nu,\max}/4\pi D^2$, where $N_{\rm e,2} = 4\pi\ R^3\ n_1/3$ is the total number of electrons in Region 2 (shocked ISM) and D is the distance of the source.

Besides the numerical calculation of the FS as described above, we can also provide an analytical description of the main properties of the evolution and emission of the FS. Generally, the evolution includes four phases. The first is a coasting phase, in which we have $\Gamma(t) \simeq \Gamma_0$. In the second phase, the shell starts to decelerate at the deceleration time

$$t_{\rm dec} = \left(\frac{3E_{\rm K,iso}}{16\pi n_1 m_{\rm p}\Gamma_0^8 c^5}\right)^{1/3}, \tag{11}$$

when the mass m of the ISM swept by FS is about $1/\Gamma_0$ of the rest mass in the ejecta $M_{\rm ej}$. After $t_{\rm dec}$, the shell approaches the Blandford & McKee (1976) self-similar evolution $\Gamma(t) \simeq (17E_{\rm K,iso}/1024\pi n_1 m_{\rm p}c^5t^3)^{1/8}$ and $R(t) \simeq (17E_{\rm K,iso}t/4\pi n_1 m_{\rm p}c)^{1/4}$. Later, the ejecta is decelerated to the post-jet-break phase at the time

$$t_{\rm j} \simeq 0.6{\rm day}\left(\frac{\theta_{\rm j}}{0.1{\rm rad}}\right)^{8/3}\left(\frac{E_{\rm K,iso}}{10^{53}{\rm erg}}\right)^{1/3} n_1^{-1/3}, \tag{12}$$

when the $1/\Gamma$ cone becomes larger than $\theta_{\rm j}$. Finally, the blast wave enters the Newtonian phase when it has swept up the ISM with the total rest mass energy comparable to the energy of the ejecta. The dynamics are described by the well-known Sedov–Taylor solution. The synchrotron flux can be described by a

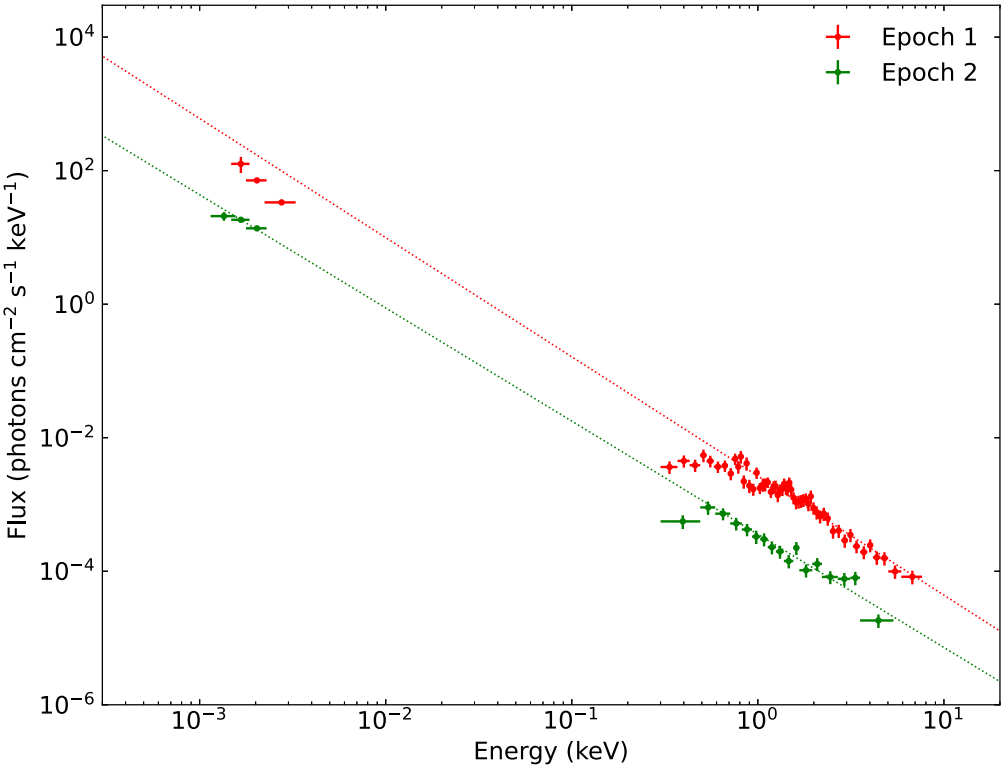

Figure 7. The afterglow SED of GRB 190106A at 28.8 ks (epoch 1, red lines) and 147.6 ks (epoch 2, green lines) from optical to X-ray. The optical multiband data are adopted from Izzo et al. (2019) and Dichiara et al. (2019). The dotted lines represent the results of a single power-law fit (dotted lines) for each epoch. The best-fit photon indexes are $\Gamma = -1.78 \pm 0.03$ (epoch 1) and $\Gamma = -1.79 \pm 0.01$ (epoch 2).

series of power-law segments $F_\nu \propto t^{-\alpha}\,\nu^{-\beta}$ (Sari et al. 1998; Gao et al. 2013). For example, in the second phase (deceleration phase), $\Gamma \propto t^{-3/8}$ and $R \propto t^{1/4}$, one has the scalings for FS spectra parameters, i.e., $\nu_m \propto t^{-3/2}$, $\nu_c \propto t^{-1/2}$ and $F_{\nu,\max,f} \propto t^0$ (Gao et al. 2013, see Equation (49) therein). In the regime $\nu_a < \nu_m < \nu < \nu_c$, one has $F_{\nu,f} = F_{\nu,\max,\,f}(\nu/\nu_m)^{-\frac{p_f-1}{2}} \propto t^{-\frac{3(p_f-1)}{4}}\nu^{-\frac{p_f-1}{2}}$. In the regime $\nu_a < \nu_m < \nu_c < \nu$, one has $F_{\nu,f} = F_{\nu,\max,\,f}(\nu_c/\nu_m)^{-\frac{p_f-1}{2}}(\nu/\nu_c)^{-\frac{p_f}{2}} \propto t^{-\frac{3p_f-2}{4}}\nu^{-\frac{p_f}{2}}$ (Gao et al. 2013, see Table 13 therein).

The RS model is described in Kobayashi (2000). In the thin shell case, the RS is Newtonian $\bar{\gamma}_{34} \sim 1$. The Lorentz factor of the shocked shell γ_3 is nearly constant during the shock crossing the shell. The shell begins to spread around $R_s = \Gamma_0^2\Delta_0$. The scalings before RS crossing time $t_{\rm dec}$ are (Kobayashi 2000).

$$\gamma_3 \sim \Gamma_0,\ n_3 = (4\bar{\gamma}_{34}+3)n_4 \sim 7n_1\Gamma_0^2(t/t_{\rm dec})^{-3},\quad e_3 \sim 4\Gamma_0^2 n_1 m_p c^2,\ N_{e,3} \sim N_0(t/t_{\rm dec})^{3/2}, \tag{13}$$

where $N_0 = M_{\rm ej}/m_p$ is the total number of electrons in the ejecta.

We also assume that electrons are accelerated at the RS front to a power-law distribution $N(\gamma_e) \propto \gamma_e^{-p_r}$, a fraction $\epsilon_{e,r}$ of the shock energy e_3 is distributed into electrons, and a fraction $\epsilon_{B,f}$ to the magnetic field in Region 3. Following a similar procedure as that used for the FS, we can obtain the scalings for parameters in the RS synchrotron spectrum (Gao et al. 2013, see Equation (26) therein),

$$\nu_a \propto t^{\frac{6p_r-7}{p_r+4}},\ \nu_m \propto t^6,\ \nu_c \propto t^{-2},\ F_{\nu,\max,r} \propto t^{3/2}. \tag{14}$$

In the regime $\nu_m < \nu_a < \nu < \nu_c$, one has $F_{\nu,r} = F_{\nu,\max,r}(\nu/\nu_m)^{-\frac{p_r-1}{2}} \propto t^{3p_r-3/2}$.

After the RS crosses the shell, i.e., $t > t_{\rm dec}$, the Lorentz factor of the shocked shell may be assumed to have a general power-law decay behavior $\gamma_3 \propto r^{-g}$. The shell expands adiabatically in the shell's comoving frame. The dynamical behavior in Region 3 is expressed with the scalings (with $g \sim 2$),

$$\gamma_3 \propto t^{-2/5},\ n_3 \propto t^{-6/7},\ e_3 \propto t^{-8/7},\ N_{e,3} = N_0. \tag{15}$$

In the same way, we can obtain the scalings for parameters in the RS synchrotron spectrum for $t > t_{\rm dec}$ (Gao et al. 2013, see Equation (31) therein),

$$\nu_a \propto t^{-102/175},\ \nu_m \propto t^{-54/35},\ \nu_{\rm cut} \propto t^{-54/35},\ F_{\nu,\max,r} \propto t^{-34/35}, \tag{16}$$

where $\nu_{\rm cut}$ is the cutoff frequency. After RS crossing, no new electrons are accelerated, nu_c will be replaced with $\nu_{\rm cut}$. In the regime $\nu_a < \nu_m < \nu < \nu_{\rm cut}$, one has $F_{\nu,r} = F_{\nu,\max,\,r}(\nu/\nu_m)^{-\frac{p_r-1}{2}} \sim t^{-\frac{27p_r+7}{35}}$.

In this section, we show that the double-peak optical light curve as well the X-ray observations of GRB 190106A can be well explained by synchrotron emission from RSs and FSs with late-time energy injection. We adopt a numerical code

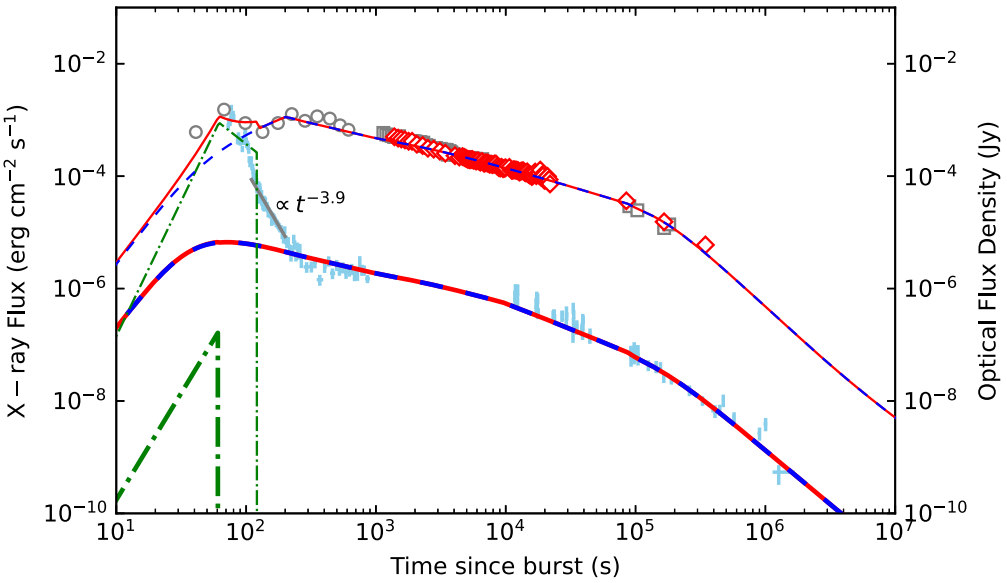

Figure 8. The modeling of X-ray (thick lines) and optical *R*-band (thin lines) light curves. Observational data are presented with circles for optical (*R* band) and pluses for X-ray. The blue-dashed lines represent emission from FS, while the green dotted–dashed lines represent RS. The combined emission from FS and RS are shown with red solid lines. The parameters adopted are listed in Table 5.

Table 5
Values of Parameters Adopted for Interpreting the Broadband Data of GRB 190106A

FS Parameters						
$E_{\rm K,iso}$ (erg)	Γ_0	n_1 (cm^{-3})	$\theta_{\rm j}$ (deg)	$\epsilon_{\rm e,f}$	$\epsilon_{\rm B,f}$	$p_{\rm f}$
9.0×10^{52}	300	4.2	0.1	0.26	0.001	2.07
RS parameters						
	$\epsilon_{\rm e,r}$	$\epsilon_{\rm B,r}$	$p_{\rm r}$			
	0.002	0.09	2.1			
Energy injection parameters						
	$L_{\rm inj}^0$(erg s^{-1})	q	$t_{\rm start}(1+z)$(s)	$t_{\rm end}(1+z)$(s)		
	0.45×10^{50}	0.05	300	1500		

described above for both the FS and RS to model the multiband observational data. The modeled X-ray and optical light curves corresponding to the abovementioned parameters (i.e., kinetic energy $E_{\rm K,iso}$, initial Lorentz factor Γ_0 and opening angle of the relativistic shell, microphysics parameters for the FS ($\epsilon_{\rm e,f}$,$\epsilon_{\rm B,f}$,$p_{\rm f}$) and RS ($\epsilon_{\rm e,r}$,$\epsilon_{\rm B,r}$,$p_{\rm r}$), and energy injection parameters ($L_{\rm inj}$,q,$t_{\rm start}$, $t_{\rm end}$) are displayed in Figure 8. However, these model parameters still suffer degeneracy when fitting the optical and X-ray data. In this work, we do not attempt to fit the data across a large parameter space. We present a set of parameter values that interpret the data well, as shown in Table 5. The subscripts "f" and "r" denote the FS and RS emission, respectively.

4.3.1. Early Double-peak Optical Light Curve

Zhang et al. (2003) pointed out that, depending on parameters, there are two types of early optical light curves for a fireball interacting with a constant-density ISM, that is, *rebrightening*, in which a distinct RS peak (with $\alpha_{\rm rise}=-3p_{\rm r}+3/2$ and $\alpha_{\rm decay}=(27p_{\rm r}+7)/35$, see the description of RS model above and also Tables 4 and 5 in Gao et al. 2013) and FS peak ($\nu_{\rm m,f}$ crossing peak) are detectable, and *flattening*, in which the FS peak is buried beneath the RS peak. The early optical light curve during the time span ∼40–1000 s post-trigger shows a double-peak feature, which is clearly a rebrightening case.

The first bump (∼40–133 s) with rising temporal index $\alpha_O=-1.88\pm0.57$ and decay index $\alpha_O=1.35\pm0.32$ can be interpreted as the combinations of an RS peak (see the blue-dashed line in Figure 8) and FS emission (see the blue-dotted line in Figure 8). We find the results with $p_{\rm r}=2.1$ can roughly explain such a bump.

The first peak is also the RS crossing time (or deceleration time) $t_{\rm decl.}$. We can estimate the initial Lorentz factor $\Gamma_0\sim300$, if we put $E_{\rm K,iso}=9\times10^{52}$ erg and $n_1=0.1\,{\rm cm}^{-1}$ into Equation (11).

The second peak (∼133.8 s) of the optical light curve occurs when the typical synchrotron frequency $\nu_{\rm m,f}$ crosses the observed frequency (Sari et al. 1998). The slow-rising index $\alpha_O=-0.58\pm0.17$ of the second optical bump (∼133–1000 s) is consistent with emission below ν_m in a slow-cooling scenario, i.e., $F_{\nu,\rm f}\propto t^{1/2}\nu^{1/3}$ (Gao et al. 2013, see Table 13 therein). For such FS peak ($\nu_{\rm m,f}$ crossing peak), one has $F_{\nu,\rm peak,f}=F_{\nu,\rm max,f}\propto\epsilon_{\rm B,f}^{1/2}E_{\rm K,iso}n_1^{1/2}$ (Gao et al. 2013, see Equation (49) therein). The values of jet isotropic kinetic energy $E_{\rm K,iso}$, ISM density n_1, and the microphysics parameter $\epsilon_{\rm B,f}$ are chosen to fit this peak.

4.3.2. Shallow Decay Phase

GRB 190106A shows quite a long shallow decay in both X-rays (following the sharp decay) and the optical (following the second bump). In a slow-cooling regime of the FS, we expect $F_\nu \propto \nu^{-(p_{\rm f}-1)/2} t^{-3(p_{\rm f}-1)/4}$ for $\nu_m < \nu < \nu_{\rm c}$, which corresponds to $\alpha = 3(p_{\rm f}-1)/4 \simeq 0.8$ using $p_{\rm f} = 2.07$ (Gao et al. 2013, see Table 13 therein). Our observed values $\alpha_O = 0.63 \pm 0.01$ and $\alpha_X = 0.36 \pm 0.03$ are shallower than those expected. This phase can be understood within the standard external-shock model with nearly constant energy injection $L_{\rm inj} \propto t^{-q}$ (see Figure 8, and Xin et al. 2012 for a similar case). In Table 5, we present the parameter values that interpret the data well, i.e., the index $q \simeq 0.05$, initial injection power $L_{\rm inj}^0 \simeq 4.5 \times 10^{49}{\rm erg\ s^{-1}}$, and starting time $t_{\rm start} > 300/(1+z)$ s. The energy injection shuts off at $t_{\rm end} \sim 1500/(1+z)$ s.

There are two popular models for the energy injection, i.e., the spin-down of a magnetar and the fallback accretion onto a stellar mass black hole (BH). First, we consider a fast-spinning magnetar as the central engine. The characteristic spin-down luminosity L_0 and the characteristic spin-down timescale τ are related to the magnetar initial parameters as (Zhang & Mészáros 2001):

$$L_0 = 1.0 \times 10^{49}{\rm erg\ s^{-1}} (B_{\rm p,15}^2 P_{0,-3}^{-4} R_6^6), \quad (17)$$

$$\tau = 2.05 \times 10^3 {\rm s} (I_{45} B_{\rm p,15}^{-2} P_{0,-3}^2 R_6^{-6}). \quad (18)$$

For the NS equation of state (EoS), we adopt EoS GM1 (the radius of the magnetar $R = 12.05$ km and the rotational inertia $I = 3.33 \times 10^{45}$ g cm^{-2}) as suggested by the recent studies with GRB data (Lu et al. 2015; Gao et al. 2016). Inserting $L_0 = L_{\rm inj} = 4.5 \times 10^{49}$ erg s^{-1} and $\tau \simeq 1500/(1+z)$ into the above two equations, one can thus infer a magnetar initial period of $P_0 \sim 1.7$ ms and a magnetic field $B_{\rm p} \sim 3.5 \times 10^{15}$ G.

For a BH central engine model, the hyper-accreting BH system can launch a relativistic jet via neutrino-antineutrino annihilation (Popham et al. 1999; Narayan et al. 2001; Di Matteo et al. 2002; Janiuk et al. 2004; Gu et al. 2006; Chen & Beloborodov 2007; Liu et al. 2007; Lei et al. 2009; Liu et al. 2015; Xie et al. 2016) or Blandford-Żnajek mechanism (hereafter BZ; Blandford & Znajek 1977; Li & Paczynski 2000; Lee & Kim 2000; Lei et al. 2005, 2013). The neutrino annihilation mechanism is too *dirty* to account for a GRB jet (Lei et al. 2013; Xie et al. 2017). For this reason, we suppose that the energy injection is dominated by the BZ mechanism. The BZ power can be rewritten as a function of mass accretion rate as (Lei et al. 2013)

$$L_{\rm BZ} = 9.3 \times 10^{53} \frac{a_\bullet^2 \dot{m} F(a_\bullet)}{(1+\sqrt{1-a_\bullet^2})^2} {\rm erg\ s^{-1}}, \quad (19)$$

where $\dot{m} \equiv \dot{M}/(M_\odot {\rm s^{-1}})$ is the dimensionless accretion rate, $a_\bullet = J_\bullet c/(GM_\bullet^2)$ is the spin parameter of the BH, $F(a_\bullet) = [(1+q_a^2)/q^2][(q_a + 1/q_a)\arctan q_a - 1]$, and $q_a = a_\bullet/(1+\sqrt{1-a_\bullet^2})$. Assuming $a_\bullet = 0.9$, the peak accretion rate is $\dot{M} \simeq 1.4 \times 10^{-4} M_\odot {\rm s^{-1}}$.

As we can see, both central engine models can give rise to the energy injection required. However, a fallback accreting BH tends to produce a giant bump in GRB afterglow light curves (Wu et al. 2013). The plateau phase is a natural expectation from a magnetar central engine (Zhang & Mészáros 2001; Lu et al. 2015). The small injection index $q \simeq 0.05$ (as shown in Table 5) favors the magnetar model.

4.3.3. Late Decay Phase

As shown in Table 3, just after the shallow decay phase, a break appears in X-ray at $1.6^{+0.7}_{-0.7} \times 10^4$ s and in the optical light curve at $7.7^{+1.1}_{-1.1} \times 10^4$ s. Apparently, the X-ray break time is earlier than the optical. In fact, this break time is affected by a large uncertainty. In Section 4.1, the X-ray light curve is divided into three segments, i.e., steep decay, shallow decay, and late decay, as shown in Table 3. It can also be fit with a four-segment broken power law: (1) steep decay (ends at $272.9^{+10.2}_{-9.6}$ s); (2) plateau (from $272.9^{+10.2}_{-9.6}$ s to $1.36^{+0.28}_{-0.90} \times 10^4$ s); (3) normal decay (from $1.36^{+0.28}_{-0.90} \times 10^4$ s to $1.0^{+0.4}_{-0.4} \times 10^5$ s); and (4) late decay (starting from $1.0^{+0.4}_{-0.4} \times 10^5$ s).[27] In such case, the X-ray break time ($1.0^{+0.4}_{-0.4} \times 10^5$ s) is roughly consistent with optical ($7.7^{+1.1}_{-1.1} \times 10^4$ s). Therefore, the X-ray and optical breaking simultaneously cannot be ruled out.

The FS model predicts temporal indices of $\alpha_O = 3(p_{\rm f}-1)/4$ and $\alpha_X = (3p_{\rm f}-2)/4$ for optical and X-rays at late times, respectively, which correspond to $\alpha_O = 0.8$ and $\alpha_X = 1.0$ using $p_{\rm f} = 2.07$ (Gao et al. 2013, see Table 13 therein). Our observed values $\alpha_{O,{\rm late}} = 1.29 \pm 0.06$ and $\alpha_{X,{\rm late}} = 1.31 \pm 0.03$ are larger than those expected.

Assuming that this break is due to the jet break, the predicted temporal index will become $\alpha_O = 1.5$ and $\alpha_X = 1.7$ by adopting $p_{\rm f} = 2.07$. As shown in Figure 8, our model can roughly fit the late-time optical and X-ray light curves. Using this jet break time, we can estimate the opening angle $\theta_{\rm j} \sim 3.^\circ 3$ if we inset $E_{\rm K,iso} = 9 \times 10^{52}$ erg, $n_1 = 0.1\ {\rm cm^{-1}}$ and $t \simeq 7 \times 10^4/(1+z)$ s into the analytical expression Equation (12). As shown in Table 5, our numerical modeling gives the opening angle $\theta_{\rm j} \sim 4.^\circ 2$, which is slightly larger than this analytical estimation.

5. Discussion

With the redshift measurement in this work, we tested the GRB by using two well-known relations, namely the Amati (Amati et al. 2002; Amati 2006) and Yonetoku (Yonetoku et al. 2004) relations, as shown in Figure 9, left and right panel, respectively. The positions of the burst lie within the 68% prediction regions, consistent with both te Amati and Yonetoku relations, which is also mentioned by Tsvetkova et al. (2019). The result suggests that GRB 190106A is a typical type II GRB.

The early double-peak optical light curve was expected by Zhang et al. 2003. We show that GRB 190106A is a good case with RS-FSs, just like GRB 041219A (Fan et al. 2005) and GRB 110205A (Zheng et al. 2012). Such a double-peak (*rebrightening*) light curve is typical for RS+FS emission combinations in a homogeneous ISM case (Zhang et al. 2003; Kobayashi & Zhang 2003). The rising temporal index

[27] https://www.swift.ac.uk/xrt_live_cat/00882252/

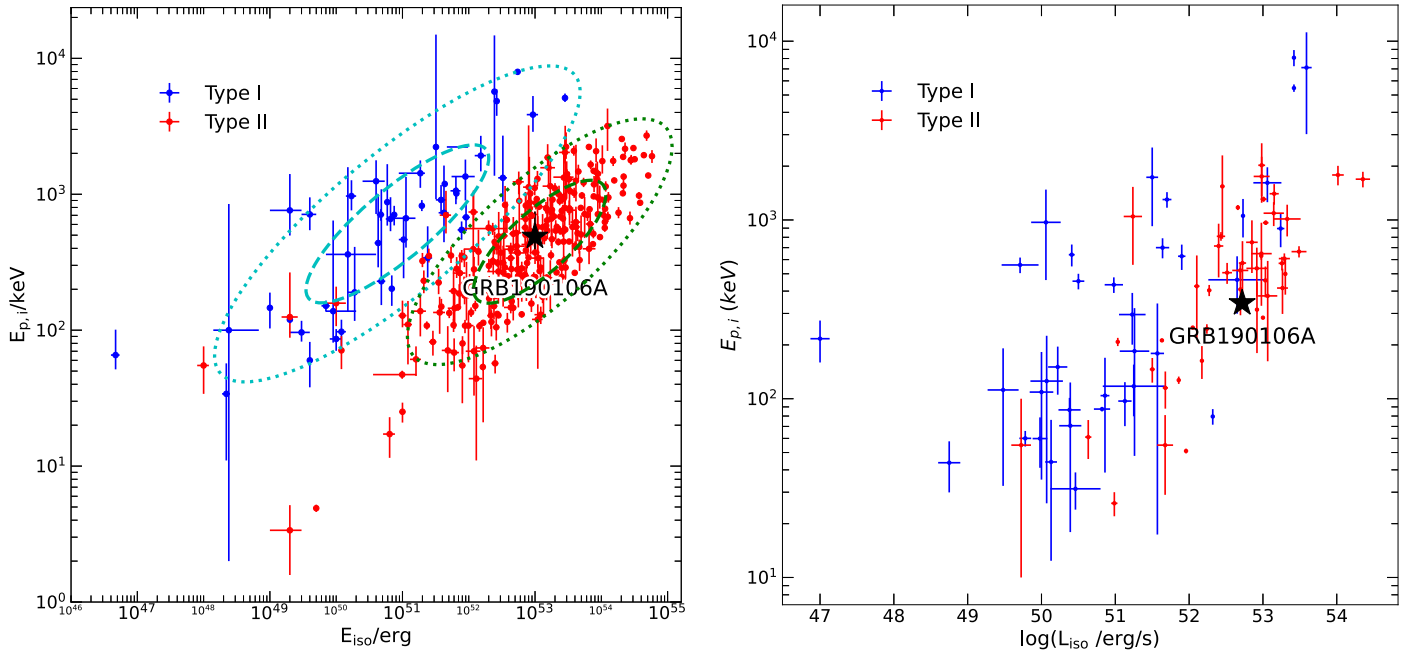

Figure 9. Left panel: Amati diagram of GRB 190106A (black star). Dashed and dotted lines represent 1σ and 2σ confidence levels, respectively. The ellipses colored in cyan and green represent type I and type II burst confidence, respectively. The data points for type I and type II GRBs are taken from Minaev & Pozanenko (2020). The burst lies within the 1σ confidence region of type II bursts, consistent with the E_p–E_{iso} correlation. Right panel: Yonetoku diagram of GRB 190106A (black star). The data points for type I and type II GRBs are taken from Nava et al. (2012) and Zitouni et al. (2022).

$\alpha_O = -1.88 < -1/2$ favors the RS in the thin-shell regime. Therefore, we adopted a thin-shell RS-FS model in a constant ISM case to investigate GRB 190106A. In this scenario, the first optical peak (RS peak) gives the fireball deceleration time (Zhang et al. 2003), which can be used to estimate the initial Lorentz factor of the GRB, $\Gamma_0 \simeq 300$. The second optical peak appears when ν_m crosses the optical band. This peak flux can be used to constrain the values of jet isotropic kinetic energy $E_{K,iso}$, ISM density n_1, and the microphysics parameter $\epsilon_{B,f}$. Based on the fit with this scenario, we infer that the magnetic field strength ratio in RS and FS is $B_r/B_f \sim 9.5$, suggesting a magnetic flux carried by the ejecta from the central engine. Therefore, a magnetized central engine model, i.e., a BH central engine powered by the BZ process or a magnetar central engine, is preferred in GRB 190106A.

It is worth noting that the first optical peak, like GRB 041219A, can be interpreted with an RS (Fan et al. 2005), internal shocks (Vestrand et al. 2005; Wei 2007), or tail emission (Panaitescu 2020). The last two models assume that the prompt optical and γ-ray emissions have a common origin. However, the radiation mechanism for the prompt γ-ray emission is still poorly understood (Kumar & McMahon 2008).

The shallow decays in both X-ray and optical bands demand a nearly constant late-time energy injection with $L_{inj} \simeq 4.5 \times 10^{49}\,\mathrm{erg\,s^{-1}}$ and $q \sim 0.05$ lasting from $\sim$300 to $\sim$1500 s. We investigated several energy injection sources, such as the spin-down of a magnetar, hyper-accreting BH powered by neutrino annihilation, and BH powered by the BZ mechanism. The neutrino annihilation mechanism is less efficient for powering the jet at a shallow decay phase. Both the magnetar and BH central engine with the BZ mechanism can give rise to the energy injection required. In general, the flat light curve feature favors the magnetar central engine model. A BH-accreting central engine can also make a flat light curve, but requires a very small value of viscosity parameter (and thus a very slow accretion) (Lei et al. 2017). On the other hand, the disk will be dominated by advection and contains a strong wind at its afterglow phase. The light curve will then become steeper due to the suppression by the wind (Lei et al. 2017).

In Section 4.1, we divided the X-ray light curve into three stages (steep decay, shallow decay, and late decay). As a result, the break time between shallow decay and late decay in X-ray is significantly different from that in the optical band ($1.6^{+0.7}_{-0.7} \times 10^4$ versus $7.7^{+1.1}_{-1.1} \times 10^4$ s), as shown in Table 3. However, the X-ray break time will be roughly consistent with the optical if we fit the X-ray light curve with four segments (steep decay, plateau, normal decay, and late decay). Considering this uncertainty, we attribute such a break to the jet break, revealing an opening angle of $\sim 4.^{\circ}2$. From the observations and modeling, we found that the total jet energy is $E_{total} = E_{\gamma,iso} + E_{K,iso} \simeq 1.9 \times 10^{53}$ erg. The opening angle-corrected jet energy will be $E_j \sim 5 \times 10^{50}$ erg, which is well below the maximum rotational energy of 3×10^{52} erg (Lattimer & Prakash 2016) -7×10^{52} erg (Haensel et al. 2009) for a standard neutron star with mass $M \sim 1.4\,M_\odot$. Therefore, our data do not require a BH as the central engine of this GRB.

6. Summary

We present our optical observation of the afterglow of GRB 190106A with the NEXT telescope, and the Xinglong 2.16 m telescope equipped with BFOSC. With the spectrum obtained from BFOSC, we measured the redshift of the burst and calculated the LSP. The unusual optical light curve obtained by NEXT and Xinglong 2.16 m, combined with the MASTER observations, shows a normal decay light curve with an early double peak and late break. Therefore, the optical light curve can be divided into five stages: rapid rise in the early stage, followed by decay, then a slow rise reaching a second peak at around 200 s, followed by a shallow decay (plateau), and faster

decay from about 1 day onward. The evolution of the X-ray light curve can be divided more simply into three stages: rapid decay, plateau, and normal decay.

The multiband observations, especially the early optical data of GRB 190106A, provide rich information to study the nature of GRB. It is found that GRB 190101A can be successfully explained by the RS-FS model. Our conclusions are summarized as follows:

1. The redshift of the burst is $z = 1.861 \pm 0.002$. The LSP is very similar to the average value of the sample.
2. The studies with the Amati and Yonetoku diagrams indicate that GRB 190106A is a typical type II burst.
3. The early double-peak optical light curve can be well interpreted with the combination of the RS and FS models.
4. The modeling with RS and FS models indicate that the magnetic field strength ratio in RS and FS is $B_r/B_f \sim 9.5$, suggesting a magnetic flux carried by the ejecta from the central engine. This favors a strongly magnetized central engine model, such as a magnetar central engine model or a BH central engine powered by the BZ process.
5. The initial Lorentz factor can be estimated with the first optical peak time (or deceleration time) as $\Gamma_0 \sim 300$.
6. The multiband afterglow data can be interpreted with the external-shock model. From the observations and modeling, we found that the total jet energy is $E_{\rm total} = E_{\gamma,\rm iso} + E_{\rm K,iso} \simeq 1.9 \times 10^{53}$ erg.
7. The shallow decays in both the X-ray and optical bands are explained by nearly constant late-time energy injection with $L_{\rm inj} \simeq 4.5 \times 10^{49}\,{\rm erg\,s^{-1}}$ and $q \sim 0.05$ lasting for $\sim$1000 s. Both magnetar and BH central engine models can give rise to such an amount of injected energy, but the flat light-curve feature favors a magnetar central engine.
8. The breaks at a few $\times 10^4$ s in both X-ray and optical bands are roughly consistent with the jet break, revealing an opening angle of $\sim 4.^\circ 2$. The opening angle-corrected jet energy will be $E_j \sim 5 \times 10^{50}$ erg.

We are very grateful to Yong Ma for the help with the NEXT observations. We acknowledge the support of the staff of the Xinglong 2.16 m telescope. This work was also partially supported by the Open Project Program of the Key Laboratory of Optical Astronomy, National Astronomical Observatories, Chinese Academy of Sciences. This work is supported by the National Key R&D Program of China (Nos. 2020YFC2201400), the National Natural Science Foundation of China under grants U2038107, U1931203, and 12021003. D.X. acknowledges support by the science research grants from the China Manned Space Project with Nos. CMS-CSST-2021-A13 and CMS-CSST-2021-B11. W.H.L. and H.G. acknowledge the support by the science research grants from the China Manned Space Project with No. CMS-CSST-2021-B11. W. Xie acknowledges support from the Guizhou Provincial Science and Technology Foundation (grant No. QKHJC-ZK [2021] 027). H.G. acknowledges support from the National SKA Program of China (grant No. 2022SKA0130101). J.Z.L. acknowledges the science research grants from the China Manned Space Project with No. CMS-CSST-2021-A08. Data resources are supported by the China National Astronomical Data Center (NADC) and the Chinese Virtual Observatory (China-VO). This work is supported by the Astronomical Big Data Joint Research Center, co-founded by the National Astronomical Observatories, the Chinese Academy of Sciences, and the Alibaba Cloud. We acknowledge the use of public data from the Swift data archive.

Software: Astrometry.net (Lang et al. 2010), Astropy (Astropy Collaboration et al. 2022), IRAF (Tody 1986), Matplotlib (Hunter 2007), NumPy (Harris et al. 2020), Python (Van Rossum & Drake 2009), SciPy (Virtanen et al. 2020), Source Extractor (Bertin & Arnouts 1996)

ORCID iDs

Zi-Pei Zhu https://orcid.org/0000-0002-9022-1928
Dong Xu https://orcid.org/0000-0003-3257-9435
Johan P. U. Fynbo https://orcid.org/0000-0002-8149-8298
Shuo Xiao https://orcid.org/0000-0003-2957-2806
Wei Xie https://orcid.org/0000-0001-5553-4577
Yuan-Chuan Zou https://orcid.org/0000-0002-5400-3261
He Gao https://orcid.org/0000-0002-3100-6558
Dieter Hartmann https://orcid.org/0000-0002-8028-0991
Antonio de Ugarte Postigo https://orcid.org/0000-0001-7717-5085
David Alexander Kann https://orcid.org/0000-0003-2902-3583
Massimo Della Valle https://orcid.org/0000-0003-3142-5020
Pall Jakobsson https://orcid.org/0000-0002-9404-5650
Tayyaba Zafar https://orcid.org/0000-0003-3935-7018
Li-Ping Xin https://orcid.org/0000-0002-9422-3437
Xing Gao https://orcid.org/0000-0002-7292-3109
Wei-Hua Lei https://orcid.org/0000-0003-3440-1526

References

Abbott, B. P., Abbott, R., Abbott, T. D., et al. 2017a, PhRvL, 119, 161101
Abbott, B. P., Abbott, R., Abbott, T. D., et al. 2017b, ApJL, 848, L12
Abolfathi, B., Aguado, D. S., Aguilar, G., et al. 2018, ApJS, 235, 42
Ahumada, T., Singer, L. P., Anand, S., et al. 2021, NatAs, 5, 917
Amati, L. 2006, MNRAS, 372, 233
Amati, L., Frontera, F., Tavani, M., et al. 2002, A&A, 390, 81
Astropy Collaboration, Price-Whelan, A. M., & Lim, P. L. 2022, ApJ, 935, 167
Atteia, J.-L., Heussaff, V., Dezalay, J.-P., et al. 2017, ApJ, 837, 119
Barthelmy, S. D., Barbier, L. M., Cummings, J. R., et al. 2005, SSRv, 120, 143
Belkin, S., Klunko, E., Pozanenko, A., et al. 2019a, GCN, 23640, 1
Belkin, S., Pozanenko, A., Minaev, P., et al. 2019b, GCN, 23661, 1
Bertin, E., & Arnouts, S. 1996, A&AS, 117, 393
Blandford, R. D., & Żnajek, R. L. 1977, MNRAS, 179, 433
Blandford, R. D., & McKee, C. F. 1976, PhFl, 19, 1130
Chen, W.-X., & Beloborodov, A. M. 2007, ApJ, 657, 383
de Ugarte Postigo, A., Fynbo, J. P. U., Thöne, C. C., et al. 2012, A&A, 548, A11
Dey, A., Schlegel, D. J., Lang, D., et al. 2019, AJ, 157, 168
Di Matteo, T., Perna, R., & Narayan, R. 2002, ApJ, 579, 706
Dichiara, S., Gatkine, P., Durbak, J. M., et al. 2019, GCN, 23744, 1
Eichler, D., Livio, M., Piran, T., & Schramm, D. N. 1989, Natur, 340, 126
Evans, P. A., Beardmore, A. P., Page, K. L., et al. 2007, A&A, 469, 379
Evans, P. A., Beardmore, A. P., Page, K. L., et al. 2009, MNRAS, 397, 1177
Fan, Y. Z., Zhang, B., & Wei, D. M. 2005, ApJL, 628, L25
Fan, Z., Wang, H., Jiang, X., et al. 2016, PASP, 128, 115005
Frail, D. A., Kulkarni, S. R., Sari, R., et al. 2001, ApJL, 562, L55
Galama, T. J., Vreeswijk, P. M., van Paradijs, J., et al. 1999, A&AS, 138, 465
Gao, H., Lei, W.-H., Zou, Y.-C., Wu, X.-F., & Zhang, B. 2013, NewAR, 57, 141
Gao, H., & Mészáros, P. 2015, AdAst, 2015, 192383
Gao, H., Zhang, B., & Lü, H.-J. 2016, PhRvD, 93, 044065
Gehrels, N., Chincarini, G., Giommi, P., et al. 2004, ApJ, 611, 1005
Geng, J. J., Wu, X. F., Huang, Y. F., & Yu, Y. B. 2013, ApJ, 779, 28
Gu, W.-M., Liu, T., & Lu, J.-F. 2006, ApJL, 643, L87
Guetta, D., & Della Valle, M. 2007, ApJL, 657, L73
Haensel, P., Zdunik, J. L., Bejger, M., & Lattimer, J. M. 2009, A&A, 502, 605

Harris, C. R., Millman, K. J., van der Walt, S. J., et al. 2020, Natur, 585, 357
HI4PI Collaboration, Ben Bekhti, N., Flöer, L., et al. 2016, A&A, 594, A116
Huang, Y. F., Gou, L. J., Dai, Z. G., & Lu, T. 2000, ApJ, 543, 90
Hunter, J. D. 2007, CSE, 9, 90
Izzo, L., Kann, D. A., de Ugarte Postigo, A., Blazek, M., & Thoene, C. C. 2019, GCN, 23660, 1
Janiuk, A., Perna, R., Di Matteo, T., & Czerny, B. 2004, MNRAS, 355, 950
Kann, D. A., Klose, S., Zhang, B., et al. 2010, ApJ, 720, 1513
Kobayashi, S. 2000, ApJ, 545, 807
Kobayashi, S., & Zhang, B. 2003, ApJ, 597, 455
Kouveliotou, C., Meegan, C. A., Fishman, G. J., et al. 1993, ApJL, 413, L101
Kuin, N. P. M., & Sonbas, E. 2019, GCN, 23626, 1
Kumar, P., & McMahon, E. 2008, MNRAS, 384, 33
Lang, D., Hogg, D. W., Mierle, K., Blanton, M., & Roweis, S. 2010, AJ, 139, 1782
Lattimer, J. M., & Prakash, M. 2016, PhR, 621, 127
Lee, H. K., & Kim, H. K. 2000, JKPS, 36, 188
Lei, W.-H., Wang, D.-X., & Ma, R.-Y. 2005, ChJAS, 5, 279
Lei, W. H., Wang, D. X., Zhang, L., et al. 2009, ApJ, 700, 1970
Lei, W.-H., Yuan, Q., Zhang, B., & Wang, D. 2016, ApJ, 816, 20
Lei, W.-H., Zhang, B., & Liang, E.-W. 2013, ApJ, 765, 125
Lei, W.-H., Zhang, B., Wu, X.-F., & Liang, E.-W. 2017, ApJ, 849, 47
Li, L., Liang, E.-W., Tang, Q.-W., et al. 2012, ApJ, 758, 27
Li, L.-X., & Paczynski, B. 2000, ApJL, 534, L197
Lipunov, V., Kuznetsov, A., Gorbovskoy, E., et al. 2019, GCN, 23661, 1
Liu, T., Gu, W.-M., Xue, L., & Lu, J.-F. 2007, ApJ, 661, 1025
Liu, T., Hou, S.-J., Xue, L., & Gu, W.-M. 2015, ApJS, 218, 12
Lu, H.-J., Zhang, B., Lei, W.-H., Li, Y., & Lasky, P. D. 2015, ApJ, 805, 89
Mao, J., Xin, Y. X., Li, Y., et al. 2019, GCN, 23630, 1
Mészáros, P., & Rees, M. J. 1997, ApJ, 476, 232
Minaev, P. Y., & Pozanenko, A. S. 2020, MNRAS, 492, 1919
Narayan, R., Piran, T., & Kumar, P. 2001, ApJ, 557, 949
Nava, L., Salvaterra, R., Ghirlanda, G., et al. 2012, MNRAS, 421, 1256
Oganesyan, G., Karpov, S., Jelínek, M., et al. 2021, arXiv:2109.00010
Oganesyan, G., Nava, L., Ghirlanda, G., Melandri, A., & Celotti, A. 2019, A&A, 628, A59
Oke, J. B., & Gunn, J. E. 1983, ApJ, 266, 713
Panaitescu, A. 2020, ApJ, 895, 39
Planck Collaboration, Ade, P. A. R., Aghanim, N., et al. 2014, A&A, 571, A16
Popham, R., Woosley, S. E., & Fryer, C. 1999, ApJ, 518, 356
Rastinejad, J. C., Gompertz, B. P., Levan, A. J., et al. 2022, Natur, 612, 223
Rees, M. J., & Meszaros, P. 1992, MNRAS, 258, 41
Rossi, A., Rothberg, B., Palazzi, E., et al. 2022, ApJ, 932, 1
Sari, R., & Piran, T. 1999, ApJ, 520, 641
Sari, R., Piran, T., & Narayan, R. 1998, ApJL, 497, L17
Schady, P., Xu, D., Heintz, K. E., et al. 2019, GCN, 23632, 1
Schlafly, E. F., & Finkbeiner, D. P. 2011, ApJ, 737, 103
Sonbas, E., Barthelmy, S. D., Beardmore, A. P., et al. 2019, GCN, 23615, 1
Tody, D. 1986, Proc. SPIE, 627, 733
Tsvetkova, A., Golenetskii, S., Aptekar, R., et al. 2019, GCN, 23637, 1
van Dokkum, P. 2001, PASP, 113, 1420
Van Rossum, G., & Drake, F. L. 2009, Python 3 Reference Manual (Scotts Valley, CA: CreateSpace)
Vestrand, W. T., Wozniak, P. R., Wren, J. A., et al. 2005, Natur, 435, 178
Virtanen, P., Gommers, R., Oliphant, T. E., et al. 2020, NatMe, 17, 261
Wei, D. M. 2007, MNRAS, 374, 525
Woosley, S. E., & Bloom, J. S. 2006, ARA&A, 44, 507
Wu, X.-F., Hou, S.-J., & Lei, W.-H. 2013, ApJL, 767, L36
Xie, W., Lei, W.-H., & Wang, D.-X. 2016, ApJ, 833, 129
Xie, W., Lei, W.-H., & Wang, D.-X. 2017, ApJ, 838, 143
Xin, L. P., Pozanenko, A., Kann, D. A., et al. 2012, MNRAS, 422, 2044
Xin, L.-P., Zhong, S.-Q., Liang, E.-W., et al. 2018, ApJ, 860, 8
Xu, D., Zhu, Z. P., Wang, Y., et al. 2019, GCN, 23629, 1
Yonetoku, D., Murakami, T., Nakamura, T., et al. 2004, ApJ, 609, 935
Yurkov, V., Gabovich, A., Sergienko, Y., et al. 2019, GCN, 23641, 1
Zeh, A., Klose, S., & Hartmann, D. H. 2004, ApJ, 609, 952
Zhang, B. 2018, The Physics of Gamma-Ray Bursts (Cambridge: Cambridge Univ. Press)
Zhang, B., Fan, Y. Z., Dyks, J., et al. 2006, ApJ, 642, 354
Zhang, B., Kobayashi, S., & Mészáros, P. 2003, ApJ, 595, 950
Zhang, B., & Mészáros, P. 2001, ApJL, 552, L35
Zhang, B., Zhang, B.-B., Virgili, F. J., et al. 2009, ApJ, 703, 1696
Zhang, B.-B., Liu, Z.-K., Peng, Z.-K., et al. 2021, NatAs, 5, 911
Zhang, Q., Lei, W. H., Zhang, B. B., et al. 2018, MNRAS, 475, 266
Zheng, W., Shen, R. F., Sakamoto, T., et al. 2012, ApJ, 751, 90
Zitouni, H., Guessoum, N., & Azzam, W. 2022, Ap&SS, 367, 74
Zou, Y. C., Wu, X. F., & Dai, Z. G. 2005, MNRAS, 363, 93